

Damage characterization in SFRP using X-ray computed tomography after application of incremental and interrupted in situ quasi static tensile loading

Guruprasad Rao¹, Alexander Amirkhanov¹, Dietmar Salaberger¹, Christoph Heinzl¹, Johann Kastner¹,

¹University of Applied Sciences Upper Austria, Stelzhamerstraße 23, Austria.

Abstract

The use of short fiber reinforced polymers (SFRP) is increasing steadily in automotive and aerospace industry due to its mechanical properties and light weight. The mechanical and physical properties of SFRP depend on the geometrical characteristics of the reinforcing material. Under tensile stress various defects are induced in SFRP composites. X-ray computed tomography (XCT) is a non-destructive method for damage characterization of SFRP. It helps to understand the material behaviour under different stress conditions and to evaluate the strength of the material. The study of the evolution of various defects in SFRP composite material was conducted for damage characterisation. The composite consisted of a polyamide matrix and 30 wt. % of short glass fibers oriented 90° relative to the direction of force. Damage was induced after application of pre-determined tensile force in a quasi static method using an in situ tensile testing device. Quasi static tensile force was applied from 85% to 99 % relative to the pre-evaluated final fracture force of 462 N. Damages were analysed after every step of the force enhancement using XCT at the resolution of $(4.5 \mu\text{m})^3$ voxel edge length.

The detected defects were classified into four types: 1) fiber pull-outs, 2) fiber fractures, 3) matrix fractures and 4) fiber/matrix debondings. Fiber pullouts and matrix fractures comprised of more than 90% of all the defects detected. The maximum number of separate defect voxels were detected prior to the final fracture post the application of 90% of final fracture force. The increase in tensile force from 90% to 96% showed a corresponding 66% increase in defect volume. Higher defect density was observed in the notched region. Fiber pullouts and fiber fracture together formed the prospective plane of final specimen fracture region. Small defects critical in the initiation of damage processes such as evolving pullouts and matrix inhomogeneities were observed from 85% to 90% of the final fracture force. The classification of defects at every step after applying force helped to understand evolution of damage mechanisms in the stressed region.

Keywords: Damage characterization in SFRP, XCT, in situ tensile tests, defect classification

1 Introduction

The automotive and aeronautic industries have to comply with stringent pollution regulations regarding emissions and are always concerned regarding the overall weight reduction. Short fiber reinforced polymers provide the required compromise of light weight and possess expected thermomechanical properties [1]. Studying the type of defects developed in these polymer composites as well as their evolution is of high interest to understand the damage mechanisms of the material in detail. Quantitative assessment of evolving defects can be closely related to predictive models of damage initiation and propagation. X-ray computed tomography (XCT) is a useful non-destructive technique to observe and quantify the defects and fiber microstructures on the fracture surface and in three dimensions inside the material [2]. Cosmi et al. have investigated fatigue damage evolution in SFRP using micro-CT [3]. In this work a quasi static tensile test until fracture was performed. The fibers were extracted using an algorithm proposed by Salaberger et al. [4]. The defects were characterized into following four types: fiber pull-outs, fiber fractures, matrix fractures and fiber/matrix debondings [5].

2 Experimental

2.1 Investigated SFRP Sample

The experiment was performed on short fiber reinforced polymers (SFRP). The investigated samples were polyamide filled with glass fibres 30% wt. (PA GF30). The fiber diameter was about 20 μm . The average length of the fibers was 300 μm . The entire specimen was 70 mm in length, 3.1 mm in width and 2.1 mm in thickness. The specimen was notched using 3 mm drill at the centre. The samples were manufactured using injection moulding technique. The fiber orientation of the specimens used was 90° relative to the force direction. Pre-evaluation tensile tests were performed on three separate test specimens in order to evaluate the average force at breakage. The average tensile stress evaluated for this orientation was 56 N/mm². In accordance with those preliminary tests, incremental force steps were planned and applied using an interrupted in situ tensile test device. The applied force steps were related to the average tensile strength. After every step of force, the specimen including the ongoing damage evolution was scanned using the XCT device.

Table 1 shows the relative tensile stress applied and the specimen integrity status. The specimen broke after six force steps after the application of 99% of the average tensile strength. Figure 1 (a) shows the GE Nanotom XCT device used (b) shows the specimen clamped vertically and mounted on the tensile testing stage with the help of two vertical mounting screws. In (c) the



stage is tightly fixed and placed in the proximity to the X-ray source. The broken and unbroken test samples are shown in Figure 1 (d).



Figure 1 (a) Nanotom XCT (b) Specimen mounted on in situ tensile testing stage (c) Closed in situ tensile testing stage inside the XCT (d) Unbroken and broken PA GF test samples

2.2 In situ tensile testing stage and the method of quasi static tensile load application

The high precision in situ tensile testing stage manufactured by Deben (UK) was used. This microtest tomography tensile / compression stage is primarily designed for use within X-ray imaging machines. The maximum force possible to apply is 5 kN. The mounting of the specimen under evaluation is performed with the help of guiding screws. This ensures proper central alignment of the sample covering entire detector area. Using Deben microtest material testing in situ device and Nanotom XCT it was possible to achieve maximum resolution of $(4.5 \mu\text{m})^3$.

The quasi static force was applied using the controlled servo motorised motion of 0.2 mm per minute. The forces were applied to the sample in percentage proportion to the force at breakage evaluated previously at 56 N/mm^2 . It was noted during the breakage tests that the material had a brittle behaviour. Hence most of the defects were expected to be evolved just before breaking force. The evaluations were planned at 80%, 85%, 90%, 93%, 95% and 99%. The equivalent force steps applied were 370 N, 393 N, 416 N, 430 N, 444 N and 458 N. After application of every force step and prior to scan a wait time of 20 minutes was chosen. This was done to avoid motion artefacts induced due to relaxation effects in polymer matrix. The sample broke after achieving 458 N force and after 3 minutes of relaxation time.

Table 1: Planned force steps for specimen with 90° orientation and specimen dimensions

Orientation	90°	Relative percentage	Force applied (N)	Specimen breakage
Average breaking stress	56 N/mm^2	80%	370	-
Specimen length	70 mm	85%	393	-
Specimen width	3.9 mm	90%	416	-
Specimen thickness	2.1 mm	93%	430	-
		96%	444	-
		99%	458	yes

Figure 2 (a) shows the incremental quasi static tensile force applied in six pre-determined steps until breakage. It also shows an extension in length of the specimen after the application of every force step. Figure 2 (b) depicts the relaxation time required for force to be in quasi static condition prior to the XCT scan. The overall scan time after each force step was 251 minutes. The decrease in force during the XCT scan (ΔF) can also be seen in Figure 2 (b).

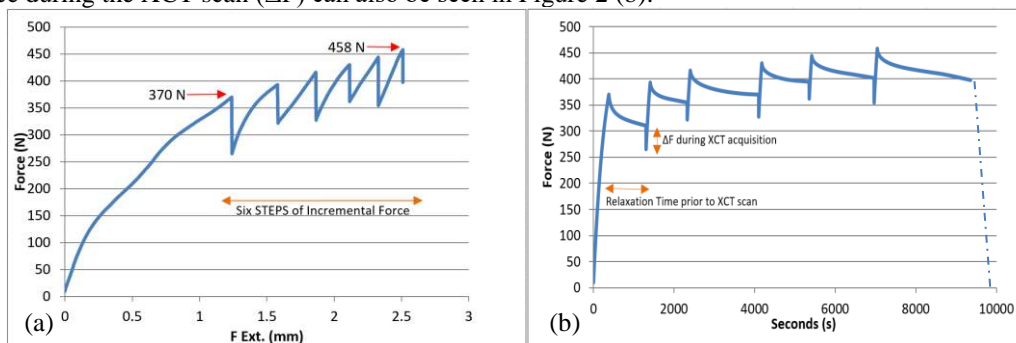


Figure 2 (a) Incremental quasi static tensile force applied to the specimen with 90° fiber orientation showing extension in length of the specimen after every force step (b) Relaxation time required for force to be in quasi static mode

2.3 Scan settings and software utilized

The force data was acquired using the Deben Microtest® V 6.0.21 software provided with the Deben in situ testing modules. XCT scans were performed on a Nanotom 180 NF device manufactured by GE phoenix|x-ray. The device uses a 180 keV nano-focus tube and a full digital 2304² pixel flat panel detector (Hamamatsu). Molybdenum was used as target material. No pre- or post-filters were used for the scans. Applied voltage on the X-ray tube was 80 kV at a voxel size of (4.5 μm)³. The reconstruction of the acquired images was performed using GE reconstruction software phoenix|Datos. XCT data processing and evaluation was done using VG Studio Max 3.0 from Volume Graphics and our in-house developed software iAnalyse v3.1.

2.4 Methodology used to detect and classify the evolving defects

The vision based inspection system can be primarily divided into four major stages. Image/Data acquisition, pre-processing, post-processing, result analyses and interpretation. The stimulus applied in this experiment was quasi static tensile force and the response of the SFRP was measured using an XCT machine.

The acquisition of the XCT data was at the resolution of (4.5 μm)³. The reconstruction was performed at a double resolution in 32 bit. The effective resolution after reconstruction was (2.25 μm)³. The 32 to 16 bit grey level mapping was done using VG StudioMax 3.0. This provided the grey level range from 0 to 65535 for every dataset acquired. Air and material grey levels were mapped at 8000 and 30000 respectively. The central notched region measuring 3 mm in height in the front view was extracted. The 3-D region was selected based upon the adaptive rectangle tool of VG StudioMax 3.0 set at ISO of 23000 and depth 14. The volume was eroded using erosion tool with strength of -2 to avoid any air regions on the border of the volume of evaluation. This data was then provided to the iAnalyse 3.1 software for further post-processing steps. After importing the data into iAnalyse the data was filtered using the gradient anisotropic diffusion filter (GADF). This was performed to remove inhomogenities in the matrix.

2.4.1 Selecting multiple OTSU (m-OTSU) as an optimum segmentation threshold

The segmentation of defects was critical component stage of the entire process. The thresholds are classified primarily into local thresholding and global thresholding. Global thresholding is widely used in many defect detection / non-destructive XCT evaluations as it is easy to implement. Different global segmentation thresholds used for various applications depending on the histograms in material sciences and region of interest. Different thresholding methods were studied for wood segmentation by Funk et. al in [6] and steel segmentation by Santanu et al. in [7]. Multi-level thresholding based segmentation for pulmonary nodules was studied by Jibi John et al. in [8]. It separated the cancerous nodules in lung CT images.

In this experiment, we have a near-unimodal histogram for the datasets. The voxels representing defects are very few and the voxels representing matrix and fibers are very high in number. OTSU method works well for the data with a clear bimodal distribution but fails at the unimodal or close to unimodal distribution as shown by Hui Fuang in [9]. It was also shown clearly by Xiao-cui Yuan in [10] and Jiu-Lun Fan et al. in [11] that the improved OTSU threshold using weighted object variance method was accurate in detecting smaller defects especially in the images with low contrast.

The data was iteratively tested using the software tool porosity analyzer developed by Weissenböck et. al [12]. ISO50, OTSU, RATS and multiple OTSU (m-OTSU) global segmentation thresholds were tested and visually compared. It was observed that m-OTSU with valley emphasis provided the best global segmentation to detect small pullouts in shortest time. Figure 3 shows small evolving pullouts segmented using m-OTSU threshold. Figure 4 (a) shows the variation in the grey levels of m-OTSU global segmentation threshold at various force levels.

2.4.2 Segmentation and post processing

The 3-D datasets were then segmented using multiple OTSU (m-OTSU) threshold with parameters as number of histogram bins = 6530 and threshold = 2. This divided the dataset into three different grey levels. Defects were mapped to 0, matrix was mapped to 1 and fibres were mapped to 2. Evolving defects are segmented as seen in Figure 3. This mask is then further binarised to generate a defect mask which includes surrounding air. This data was further processed using 4DCT tool in iAnalyse. The connected component filter from 4DCT tool was used. A labelled component image without surrounding air and sequential numbered defects was created. This served as a defect mask for defect classification. Defect visualisation tool requires following inputs 3D-filtered image of the specimen, extracted fibers, defect mask and extracted features of defects from 4DCT tool. The fiber extraction was performed using the fiber extraction tool in iAnalyse. The parameters are shown in Figure 4 (b). The defect features were extracted using 4DCT tool in iAnalyse.

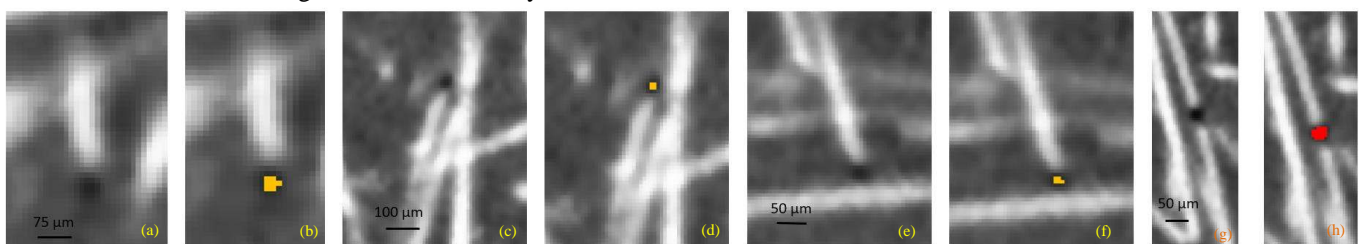


Figure 3 Small evolving defects segmented using m-OTSU global segmentation threshold (a-f) pullouts (g-h) fiber fracture

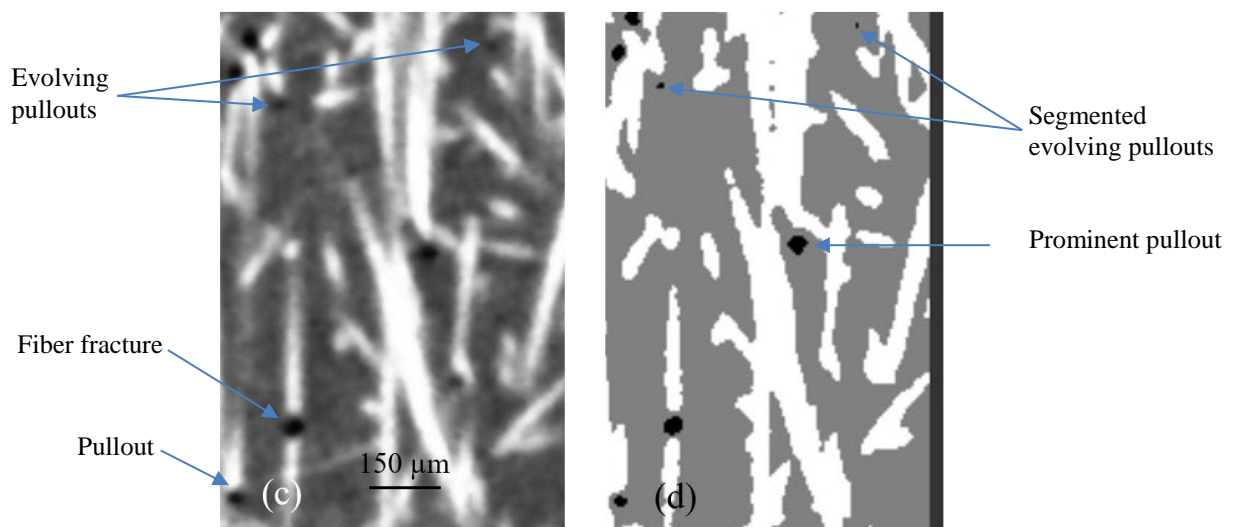
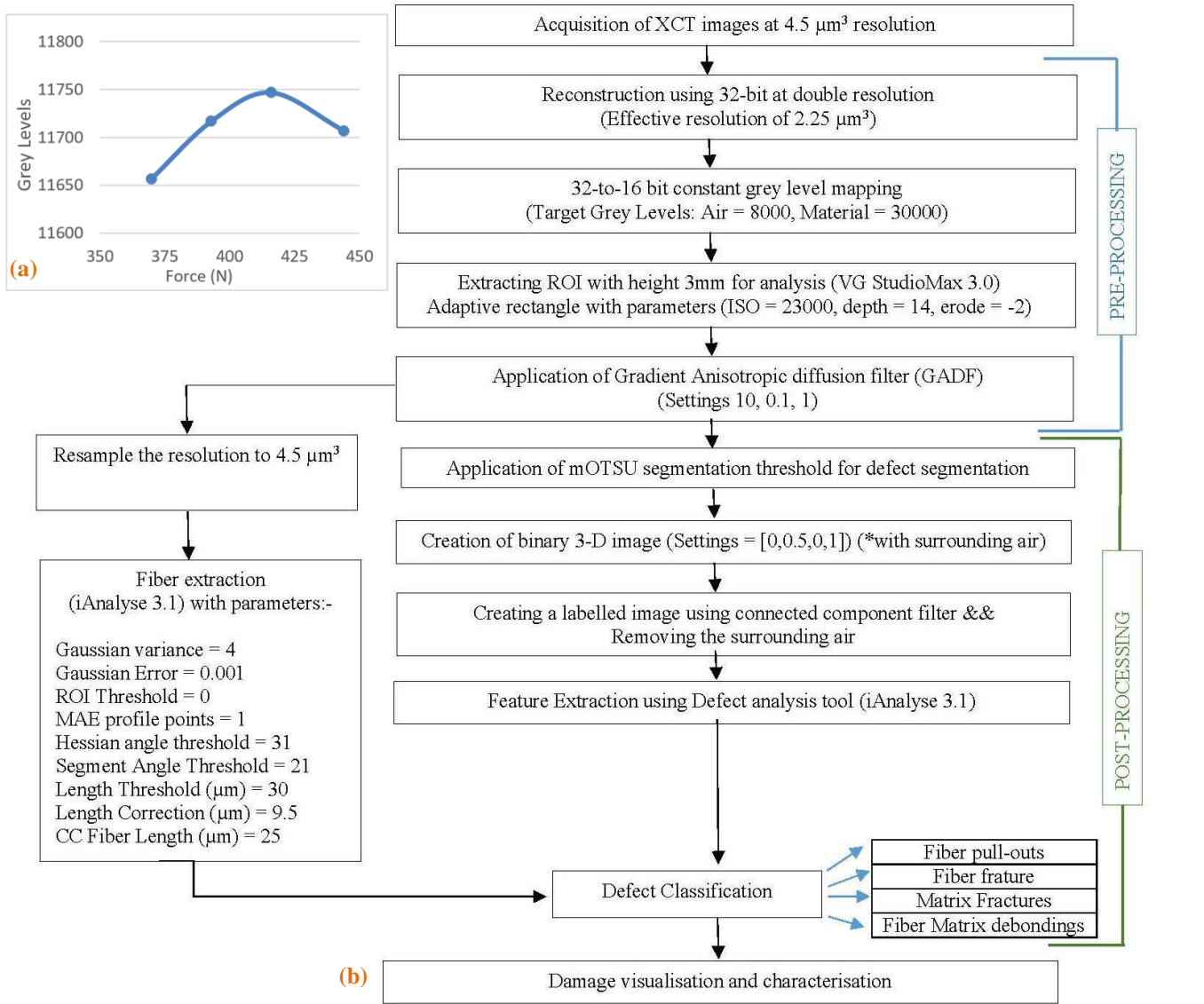


Figure 4 (a) Grey level variation in m-OTSU threshold (b) flow chart showing methodology used for damage visualization and characterization (c) filtered unsegmented image (d) m-OTSU segmented image

3 Results

3.1 Local Anisotropy in SFRP specimen

To evaluate the effect of quasi static tensile force on the individual fibers it was important to consider the orientation of the fibres along with the force applied. Local anisotropy was observed as reported in the SFRP material by Bernasconi et al in [13]. He showed the three separate regions of skin, shell and core in an injection moulded specimen have a varied orientation. The core region has the orientation different to that of surrounding shell regions. Figure 5 (a) shows the 3-D visualisation of the specimen ROI evaluated post-extraction. Figure 5 (b) shows the overall distribution of orientation of fibres in the sample. The fibers aligned in 90 degrees in the shell regions are indicated in green and fibers aligned 0 degrees in the core region are shown in blue colour. Figure 5 (c) shows the XCT slice images in the shell and core region. Figure 5 (d-f) shows CT-slice view of the orientation of fibers in the shell and core regions.

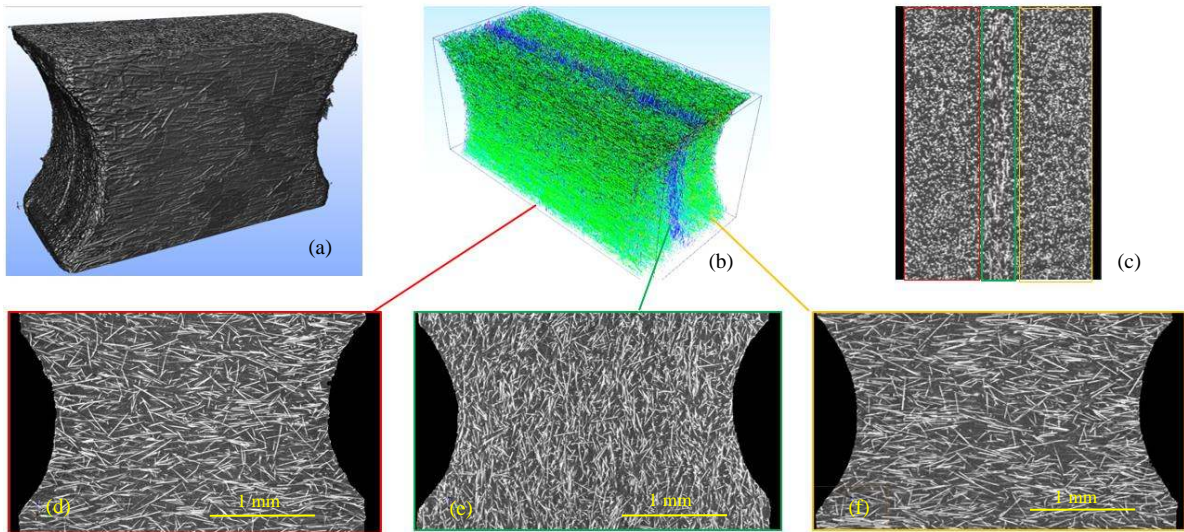


Figure 5 Fiber orientation and local anisotropy visualisation (a) 3-D volume rendering of the specimen ROI. (b) Fibers extracted; anisotropy observed in core region as compared to the shell regions (c) XCT slice image showing local anisotropy (d, f) Front and shell region fiber orientations (e) core region fiber orientation

There were primarily two orientations observed in the specimen as illustrated in Figure 6 (a). The fibers in the core region aligned in the 0 degrees and fibers in the shell region aligned in the 90 degrees. The fibers in the intermediate regions had mixed orientations. The concentration of force at fibre ends in the core region is higher as shown in Figure 6 (b). The figure illustrates the development of a pullout at increasing force steps. The surface area exposed to the direction of force is higher in the shell region as shown in Figure 6 (b). The figure illustrates the development of a fiber-matrix debonding.

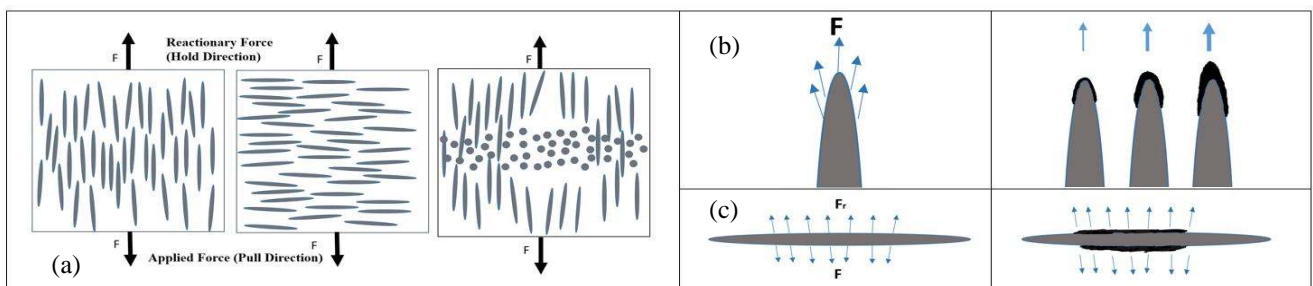


Figure 6 (a) Fiber orientation in shell and core regions (b) Force experienced at fiber ends and development of a pullout in core region (c) Force experienced at surface of the fiber in the shell region

3.2 Comparative defect classification at various Force steps

The XCT datasets corresponding to 0 N, 370 N, 393 N, 416 N and 444 N were analyzed using the flow chart given in section 2.4. In Figure 7 (a-d) progressive damage visualization at 0 N, 416 N, 430 N and 444 N is shown. The green highlighted region shows the pullouts at 416 N which combine as a connected defect at 444 N. It was observed that the final fracture occurred in the region near the edges where the separate evolving defects accumulated and increased their volume to give rise to final fracture. The red highlighted region shows a fiber fracture at 416 N. In Figure 7 Figure 7(e) the rise in number of defect voxels detected can be seen. It shows an over-all increase of defect volume as the force is increased. In Figure 7 (f) the total number of defects detected at increasing force is shown. It can be noted that the number of defects decrease significantly as the force is increased.

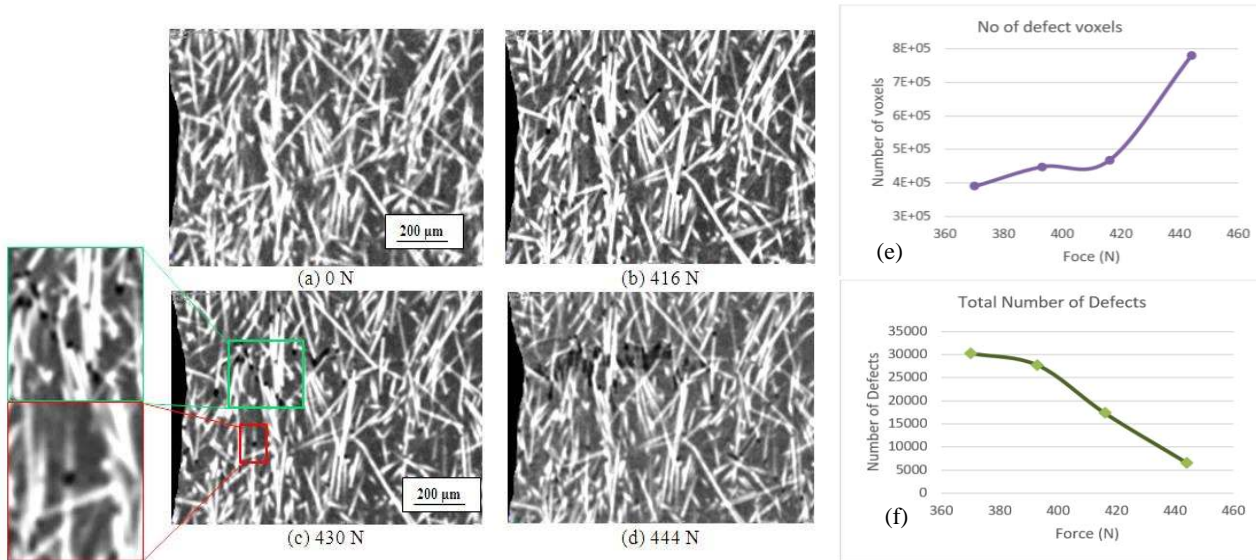


Figure 7 XCT visualization of progressive damage evolution after application of force steps for 90° orientation specimen in core region (a) 0N (b) 416 N (c) 430 N (d) 444N; green region highlights fiber cluster having pull-outs red region highlights fiber fracture

Figure 8 (a-d) shows the percentage of number of each type of defects detected at various incremental force steps from 370 N to 444 N. Figure 8 (e-f) shows the percentage of volume detected for each of the four types of defects. Figure 8 (i) shows rendered volume of the bottom part of the broken specimen. Highlighted region shows the fibers that were pulled out of the other part.

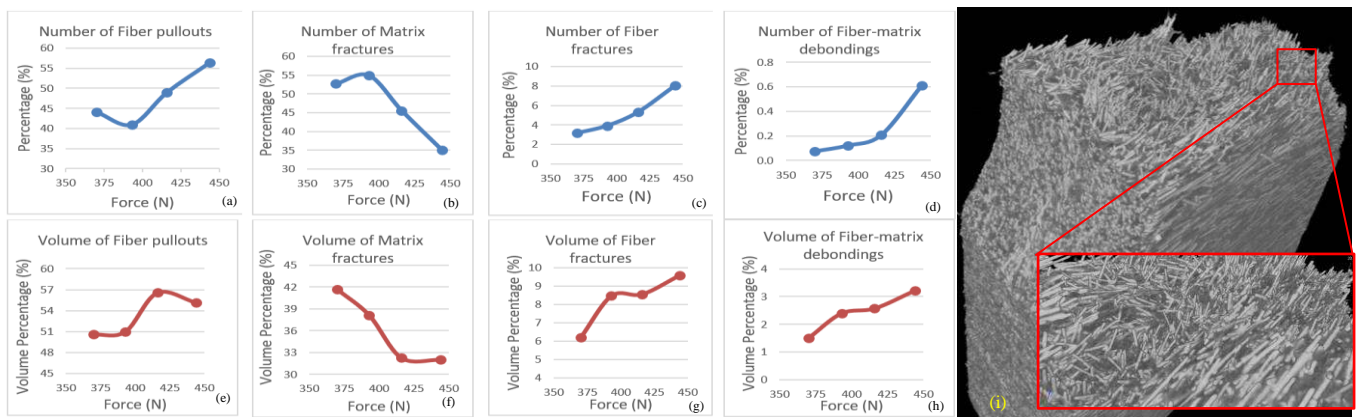


Figure 8 Comparison of various defect classes at incremental force steps for damage characterization (a-d) trend in the number of defects detected (e-h) trend showing percentage of volume detected (i) 3-D volume rendering showing fibers outside of the specimen.

4 Discussions

The process of the formation of final fracture from its initiation has many intermediate steps. Understanding the damage evolution involves quantification and visualization of all the intermediate steps in the generation of final crack. In this experiment, we were successful in segmenting and classifying different types of defects in SFRP specimen non-destructively. The overall increase in the volume of defects detected can be seen in Figure 7 (e). It was seen that the volume of the defects increased from $35.5 \times 10^6 \mu\text{m}^3$ to $71.1 \mu\text{m}^3$ as shown in the Table 2. The increase of defect volume from 370 N to 416 N is lower as compared to the increase from 416 N to 444 N. It shows that most of the defect volume surge took place between 90% to 96% of the force at final fracture. There were very few fiber-matrix debondings detected.

Figure 7 (f) shows decrease in the number of defects detected at incremental force steps. The decrease in number of defects detected from 370 N to 393 N is lower. There is a huge decrease in number of defects detected from 416N to 444 N. At the lower forces the defects detected were very small in volume. Also, there were small voxel clusters within matrix showing matrix inhomogeneities detected and classified as matrix fractures.

Table 2: Volume of the defects detected at various force steps and relative increase in percentage

Applied Force	Total volume of defects ($\times 10^6 \mu\text{m}^3$)	% increase
370	35.5	
393	40.9	15.1
416	42.6	4.36
444	71.1	66.8

4.1 Damage characterization based on the classified defects and 3-D visualization

The classified defects from 370 N to 444 N were quantified based on the percentage of number of separated defects for every type in Figure 8. The pullouts and matrix fractures together account up to the 90 % of number of defects at all force stages. There is a 4 % decrease in number of pullouts from 370 N to 393 N. This can be attributed to the large number of pullouts with volume ranging from single voxel to a few voxels at low tensile forces. The XCT artefacts induced due inhomogeneities within matrix material are classified as defects. The number of fiber fractures increase constantly from 2 % at 370 N up to 8 % at 444 N. There were very few fiber-matrix debondings detected.

The volume of each type of defects detected presents a broader understanding of the evolution of damages as shown in Figure 8 (e-h). The volume of pullouts and matrix fractures together account up to 90 % of the defects detected. There is 50 % of the defect volume initially detected which grows at a higher rate from 393 N up to 416 N and depreciates by around 2 percentage points from 416 N to 444 N. Correspondingly the volume for matrix fractures decreases from 370 N to 416 N and remains steady after further increase in force. The volume of fiber fracture rose from 6 % at 370 N to 8.5 % at 393 N. From 393 N to 416 N it was steady and showed a meagre increase of 1 percentage point at 444 N. The volume of fiber-matrix debondings is lowest from 1.5 % at 370 N to 3 % at 444 N. The volume is significantly higher relative to the number of defects detected.

Figure 9 (a) shows the 3D distribution of the various defects detected within the specimen at 416 N. Figure 9 (b) shows the concentration of defects near the notch region. Many pullouts were observed in the core region of the specimen where the orientation of the fibers is 0 degrees. Majority of the defects are small in volume as compared to the volume of total specimen. The density of the defects near the notch region is also higher as compared to the central shell regions. Also, the spread of defects signifies the probability of the final fracture plane occurrence.

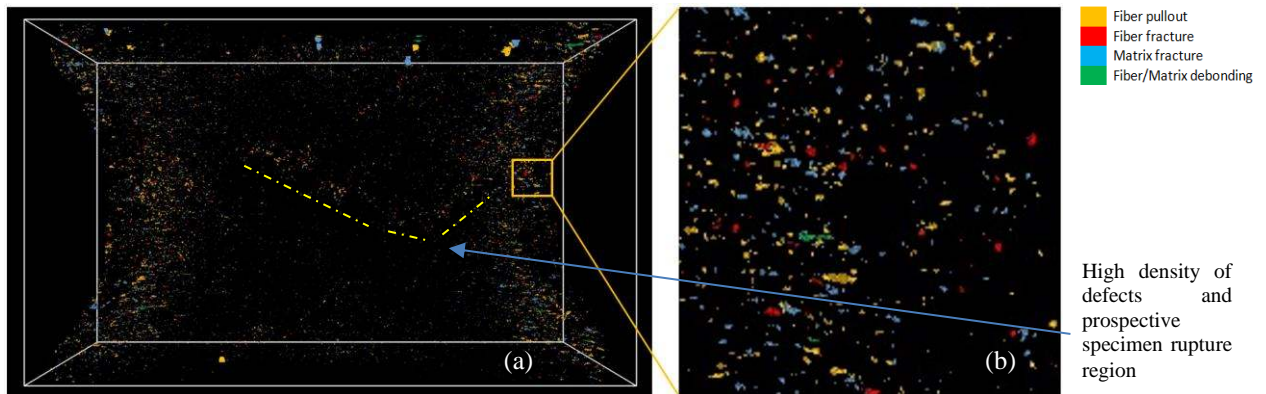


Figure 9 (a) 3-D visualization of all the classified defects detected at 416 N
 (b) Zoomed-in figure shows the dense distribution of defects at notched region

5 Conclusion and Outlook

It was noted that maximum number of defect voxels were detected after the application of 90 % of the force required for final fracture. Defect density was significantly higher in the notched region. The region with high density of defects was in proximity to the final fracture. Pullouts and matrix fractures comprised of more than 90% of the total number of defects segmented in this material system. Fiber fractures detected were comparatively less in number and occupied a higher volume. Fiber pullouts and fiber fracture together form the prospective plane of final specimen fracture region.

The efficiency of the final defect detection results depends on the overall efficiency from the acquisition step through all the intermediate pre-processing and post processing stages and finally upon the defect classification tool itself. Although XCT provides us with a great possibility to observe and evaluate the evolving defects, it suffers with certain constraints. There is an inherent distance between the X-ray source and the specimen depending upon the thickness of the in situ tube. This limits the resolution of XCT scans. There were small single/few voxel detections in the initial force steps. These were either evolving

pullouts or XCT artefacts due to uneven absorption resulting in matrix inhomogeneities. It is very decisive to remove the inhomogeneities using the gradient anisotropic filter (GADF) without losing evolving defects.

The segmentation of the small defects poses a big challenge in industrial computed tomography images with low resolution and near uni-modal histograms. Also, in the initial scans the defects evolving out of the matrix had similar grey levels to the matrix. These are important as they are the initiators of the damage mechanisms in SFRP polymers. It was observed that most of the evolving defects were segmented using the m-OTSU threshold. There was low deviation in the m-OTSU grey level threshold which establishes robustness of the segmentation methodology.

It is now possible to scan SFRP specimens non-destructively using XCT after application of quasi tensile force steps. It is also possible to visualize how the defects are evolved, to classify the type of defects and to quantify volume occupied by these defects. It helped us to observe quantitatively and qualitatively the evolving damage mechanisms in a composite SFRP structure.

Acknowledgements

The research was financed by the European Union's Seventh Framework Programme (FP7/2007-2013) under grant agreement No. 607817 (INTERAQCT: International Network for the Training of Early stage Researchers on Advanced Quality control by Computed Tomography). This work also received funding from the K-Project ZPT+ supported by COMET programme of FFG and by the federal government of Upper Austria and Styria. I would like to specially thank Johannes Weissenböck for his valuable inputs, time and discussion regarding utilization porosity analyzer.

6 References

- [1] M. F. Arif, N. Saintier, F. Meraghni, J. Fitoussi, Y. Chemiskya and G. Robert, "Multiscale fatigue damage characterization in short glass fiber reinforced polyamide-66," *Composites: Part B journal*, pp. 55-65, 2014.
- [2] T. Joffre, A. Miettinen, E. Wernersson, P. Isaksson and K. Gramsted, "Effects of defects on the tensile strength of short fiber composite materials," *Mechanics of Materials*, pp. 125-134, 2014.
- [3] F. Cosmi and A. Bernasconi, "Micro-CT investigation on fatigue damage evolution in short fibre reinforced polymers," *Composites Science and Technology*, vol. 79, pp. 70-76, 2013.
- [4] D. Salaberger, K. Kannappan and J. Kastner, "Method of the 3D characterisation of fibres in reinforced polymers," in *Industrial Computed Tomography*, Wels, 2010.
- [5] A. Amir Khanov, A. Amir Khanov, D. Salaberger, J. Kastner, E. Gröller and C. Heinzl, "Visual Analysis of Defects in Glass Fiber Reinforced Polymers for 4DCT Interrupted In situ Tests," *Eurographics conference on visualisation (Eurovis)*, vol. 35, no. 3, p. 10, 2016.
- [6] J. W. Funck, Y. Zhong, D. A. Butler, C. C. Brunner and J. B. Forrer, "Image segmentation algorithms applied to wood defect detection," *Computers and electronics in agriculture*, vol. 41, pp. 157-179, 2003.
- [7] S. Ghorai, A. Mukherjee, M. Gangadaran and P. K. Dutta, "Automatic defect detection on hot-rolled flat steel products," *IEEE Transactions on Instrumentation and Measurement*, vol. 62, pp. 612-621, 2013.
- [8] J. John and M. G. Mini, "Multilevel Thresholding Based Segmentation and Feature Extraction for Pulmonary Nodule Detection," *Procedia Technology*, vol. 24, pp. 957-963, 2016.
- [9] H.-F. Ng, "Automatic thresholding for defect detection," *Pattern recognition letters*, vol. 27, pp. 1644-1649, 2006.
- [10] X.-c. Yuan, L.-s. Wu and Q. Peng, "An improved Otsu method using the weighted object variance for defect detection," *Applied Surface Science*, vol. 349, pp. 472-484, 2015.
- [11] J. L. Fan and B. Lei, "A modified valley-emphasis method for automatic thresholding," *Pattern Recognition Letters*, vol. 33, pp. 703-708, 2012.
- [12] J. Weissenböck, A. Amir Khanov, E. Gröller, J. Kastner and C. Heinzl, "Porosity Analyzer: Visual Analysis and Evaluation of segmentation Pipelines to Determine the Porosity in Fiber-Reinforced Polymers," *IEEE Visual Analytics Science and Technology, VAST 2016*, p. 10, 2016.
- [13] A. Bernasconi, F. Cosmi and D. Dreossi, "Local anisotropy analysis of injection moulded fibre reinforced polymer composites," *Composites Science and Technology*, vol. 68, pp. 2574-2581, 2008.
- [14] A. Bernasconi, P. Davoli, A. Basile and A. Filippi, "Effect of fibre orientation on the fatigue behaviour of a short glass fibre reinforced polyamide-6," *International Journal of Fatigue*, vol. 29, pp. 199-208, 2007.